Polaron spectral properties in doped ZnO and $SrTiO_3$ from first principles

Gabriel Antonius,[1,2,3] Yang-Hao Chan,[1,2] and Steven G. Louie[1,2]
[1]*Department of Physics, University of California at Berkeley, California 94720, USA*
[2]*Materials Sciences Division, Lawrence Berkeley National Laboratory, Berkeley, California 94720, USA*
[3]*Département de Chimie, Biochimie et Physique, Institut de recherche sur l'hydrogène,*
Université du Québec à Trois-Rivières, C.P. 500, Trois-Rivières, Canada

(Received 24 August 2020; revised 31 October 2020; accepted 4 November 2020; published 1 December 2020)

We reveal polaron signatures in the spectral function of *n*-doped $SrTiO_3$ and ZnO through first-principles interacting Green's function calculations. In $SrTiO_3$ we observe a clear replica band at 94 meV below the conduction band, which shows that the observed replica in recent angle-resolved photoemission spectroscopy experiment is an intrinsic feature from electron-phonon coupling in $SrTiO_3$. In contrast, we observe an elongated tail in the spectral function for ZnO but no well-separated replicas. By increasing the electron doping level, we identify kinks in the spectral function at phonon frequencies and a decreasing intensity of the tail structure. We find that the curvature of the conduction band bottom vanishes due to additional electron-phonon scattering channels enabled by increased occupied states at high-enough doping levels, beyond which the spectral function becomes a stronger quasiparticle one with a single peak structure. We further compare the spectral function computed from the Migdal-Dyson approach and the cumulant method, and show that the cumulant method can correctly reproduce the polaronic features observed in experiments.

DOI: 10.1103/PhysRevResearch.2.043296

I. INTRODUCTION

Doped transition metal oxides such as $SrTiO_3$ (STO) and ZnO display two-dimensional electron gas (2DEG) behaviors on their surface [1–5] with a host of functional properties, such as tunable metal-to-insulator transitions [6,7], magnetism [8], and superconductivity [9,10]. The charge carriers dynamics in these systems is indicative of significant polaronic effects [11] and can be studied with angle-resolved photoemission spectroscopy (ARPES). Strong electron-phonon interaction at the origin of polaron formation in these materials is a ubiquitous feature of oxygen-rich and ionic compounds [12–14], and has been attributed to the enhancement of two-dimensional superconductivity in FeSe sheets on STO surfaces [15].

Recent ARPES measurements in doped STO [2,16], ZnO [17], and TiO_2 [18] reveal satellite bands located at distinctive phonon frequencies below the conduction band. The polaronic tail observed in these spectra is usually fitted with several multiphonon replica bands located at integer multiples of the longitudinal optical (LO) phonon frequencies. This interpretation is supported, on the one hand, by model calculations [16–18]. On the other hand, a first-principles description of quasiparticle spectral functions including electron-phonon interaction has been achieved with the cumulant expansion formalism [12,19–26]. This method was shown to accurately reproduce the position and intensity of multiphonon replica bands observed in TiO_2 [27]. When interpreting ARPES signals, however, the physics of the bulk may be concealed by surface effects and impurities.

In this work, we investigate polaronic signatures in bulk doped STO and ZnO from first principles using the cumulant expansion formalism. We find that in STO, the polaronic tail in ARPES is visible for the one-phonon process, but quickly dies off for multiphonon processes. In ZnO, the theoretical ARPES spectra do not feature a long polaronic tail. Rather, as the polaron forms with increased doping, the conduction band becomes increasingly flatten, with increased effective mass.

II. METHOD

A. Spectral function

The spectral function of the electrons, which relates closely to the observed ARPES signal, is given by $A_{n\mathbf{k}}(\omega) = \frac{1}{\pi}|\mathrm{Im}G_{n\mathbf{k}}(\omega)|$, where G is the Green's function of the electrons dressed by the electron-phonon interaction. In the Dyson equation approach, these interactions are contained in the self-energy ($\Sigma_{n\mathbf{k}}$), and the Green's function is given by

$$G_{n\mathbf{k}}(\omega) = \frac{1}{\omega - \epsilon_{n\mathbf{k}} - \Sigma_{n\mathbf{k}}(\omega) + i\eta}. \tag{1}$$

The main peaks of the spectral function correspond to the quasiparticle energies $E_{n\mathbf{k}} = \epsilon_{n\mathbf{k}} + \Sigma_{n\mathbf{k}}(E_{n\mathbf{k}})$, where $\epsilon_{n\mathbf{k}}$ are the bare electronic eigenvalues (i.e., without considering the electron-phonon interaction).

The Migdal approximation [28] consists of computing the self-energy to the lowest order in the phonon interaction.

Published by the American Physical Society under the terms of the Creative Commons Attribution 4.0 International license. Further distribution of this work must maintain attribution to the author(s) and the published article's title, journal citation, and DOI.

Using the Migdal self-energy to obtain the Green's function from Eq. (1) is known as the Migdal-Dyson formalism. This approach suffers from two important shortcomings. First, it produces only a single statellite peak in the spectral function since the self-energy at the lowest order lacks multiphonon processes. Second, the satellite peak appears at one phonon frequency away from the *bare* electronic eigenvalue ($\epsilon_{n\mathbf{k}}$), while the main quasiparticle peak energy ($E_{n\mathbf{k}}$) is also shifted away from the bare energy position in the opposite direction. This results in a separation between the quasiparticle peak and the satellite that is larger than one phonon frequency while, on physical grounds, this separation should be *exactly* one phonon frequency.

The description of the spectral function can be improved using the retarded cumulant expansion formalism. In this approach, the Green's function is expanded in terms of a cumulant function $C^R(t)$ as

$$G^R_{n\mathbf{k}}(t) = -i\theta(t)e^{-i\epsilon^0_{n\mathbf{k}}t}e^{C^R_{n\mathbf{k}}(t)}. \tag{2}$$

The cumulant function is found by imposing that, at the lowest order in phonon interaction, G^R agrees with the related G obtained from the Migdal-Dyson theory, giving

$$C^R_{n\mathbf{k}}(t) = ie^{iE_{n\mathbf{k}}t}\int\frac{d\omega}{2\pi}e^{-i\omega t}G^{0,R}_{n\mathbf{k}}(\omega)^2\Sigma^R_{n\mathbf{k}}(\omega). \tag{3}$$

The superscript R indicates that the retarded versions of the Green's function and self-energy is used, treating particles and holes on equal footing [24]. In practice, the self-energy is separated for convenience into a dynamical and a static part, the first being complex and frequency-dependent, and the second being real and frequency-independent [12]. In the above equation, $\Sigma^R(\omega)$ only refers to the dynamical part of the self-energy, while the contribution of the static part is included in Eq. (2) by setting $\epsilon^0_{n\mathbf{k}} = E_{n\mathbf{k}} + \Sigma^{\text{static}}_{n\mathbf{k}}$. Using the spectral representation of $\Sigma^R(\omega)$ yields the final form of the cumulant function [12]

$$C^R_{n\mathbf{k}}(t) = \frac{1}{\pi}\int_{-\infty}^{\infty}d\omega\frac{\left|\text{Im}\Sigma^R_{n\mathbf{k}}(\omega + E_{n\mathbf{k}})\right|}{\omega^2}(e^{-i\omega t} + i\omega t - 1). \tag{4}$$

The first term of Eq. (4) produces multiple satellite peaks in the spectral function, while the second and the third terms correspond to the quasiparticle energy shift and a renormalization constant, respectively. Here, we use the quasiparticle energy $E_{n\mathbf{k}}$ as a starting point for the cumulant expansion, as we found that it is necessary to properly describe the mass enhancement of the bands.

B. Computational details

We perform density functional theory (DFT) calculations with the ABINIT first-principles simulation package [29], and use the Perdew-Burke-Ernzerhof (PBE) pseudopotential from the PSEUDODOJO database [30]. The wave functions of STO and ZnO are described with plane-wave energy cutoffs of 70 and 50 Ha, respectively, and the ground-state densities are obtained with 8 × 8 × 8 and 6 × 6 × 6 wave vectors (**k**-points) meshes, respectively. The phonon frequencies and phonon coupling potential are computed with density functional perturbation theory (DFPT), starting with a *coarse* sampling of phonon wave vectors (**q**-points) of 8 × 8 × 8.

In the case of STO, the computation of the electron-phonon interaction is complicated by the presence of soft phonon modes at the corners of the Brillouin zone, which are responsible for a phase transition below 105 K [31–33]. Above this temperature, the cubic phase is stabilized by quantum fluctuations of the atomic positions, but the Born-Oppenheimer energy surface of the atoms remains largely anharmonic. To account for this anharmonicity, we use the temperature-dependent effective potential (TDEP) method, which describes the stabilized phonon frequencies at finite temperatures. We generate random atomic configurations in a 2 × 2 × 2 cubic cell of STO at 300 K by performing 20 000 molecular dynamics steps with a 2-fs time inverval, and sample 40 configurations out of the last 5000 steps. The effective force constants are then fitted with the ALAMODE code [34] to produce the finite-temperature phonon frequencies and polarization vectors.

C. Interpolation of the phonon coupling potential

The long-ranged nature of the electron-phonon coupling in polar materials means that the coupling strength diverges as $1/q$ for the LO phonon branches, which are characterized by large Born effective charges. As a result, the LO modes make up the dominant contribution to the electron's electron-phonon coupling self-energy (Σ^{ep}) [35]. We compute Σ^{ep} using adaptative q-point grids, defined by a *coarse* mesh and a *fine* mesh. The phonon coupling potential is interpolated onto the fine q-mesh through its real-space representation, a technique that does not require the computation of Wannier functions, which is detailed in Refs. [29,36] and we summarize as follows. The long-ranged part of the phonon coupling potential is analytic for every phonon wave vector **q**, once the Born effective charges have been computed from DFPT [36]. This long-ranged part is substracted from the phonon coupling potential to yield the short-ranged part of the potential. The short-ranged part of the phonon coupling potential is then Fourier-transformed from the coarse q-point mesh to a real-space mesh of lattice vectors of the same size as the coarse q-point mesh [37]. Assuming the short-ranged potential is zero beyond this mesh of lattice vectors, it can be Fourier-transformed back onto the fine q-point mesh, and the analytic long-ranged part is added to recover the full potential on the fine q-point mesh.

We use a fine q-point mesh of 48 × 48 × 48 to compute Σ^{ep}, and further refine our BZ sampling of the contribution of the q-space near $q = 0$ (Γ cell), to a 196 × 196 × 196 q-point mesh. This sampling allows one to resolve phonon scattering processes near the Fermi surface for all doping levels considered, which ensures the convergence of the self-energy (see the Appendix).

D. Doping

The doping is introduced in the computation of the self-energy by adjusting the Fermi level in the rigid-band approximation. We account for the extra dielectric screening contributed by the additional charge carrier density using a

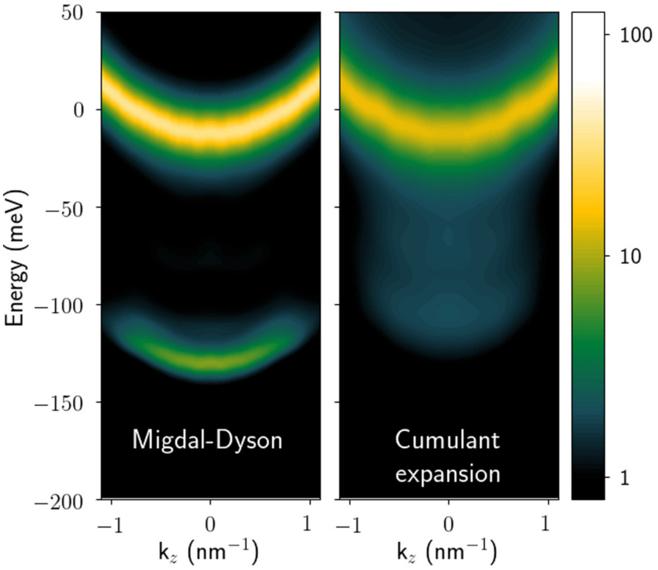

FIG. 1. Spectral function of doped $SrTiO_3$ along the Γ-*M* direction computed with the Migdal-Dyson theory (left) and the cumulant expansion method (right). The doping density is $n = 1.6 \times 10^{19}$ electrons/cm^3. The color scale is the normalized spectral function in units of states/unit cell/meV.

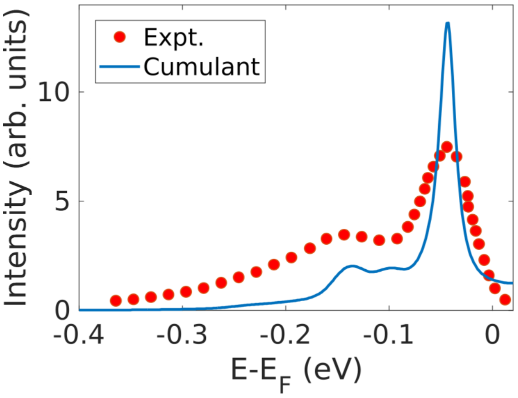

FIG. 2. Comparison of the calculated spectral function with ARPES measurements of the conduction band of $SrTiO_3$ at Γ. Blue line: The spectral function from cumulant expansion method, open circle: Experiment data from Ref. [2]. The peak position of the calculated spectral function is shifted to align with the experiment data. The background intensity is subtracted from the experimental data. The doping level is $n = 1.6 \times 10^{19}$ cm^{-3}.

model Lindhard dielectric function. This dielectric function is computed from the band structure, and further screens the electron-phonon coupling matrix elements. This model has been introduced by Verdi *et al.* [27], who used it to show that in TiO_2, the spectral function exhibits polaronic features at low doping, and transition into a Fermi-liquid behavior as the dopant concentration increases.

III. RESULTS

A. $SrTiO_3$

We fist compute the self-energy of undoped STO at zero temperature. The real part of the self-energy yields a value of −290 meV for the zero-point renormalization (reduction) of the band gap, which is in good agreement with the experimental value of −336 meV obtained from temperature-dependent absorption measurements [38]. Figure 1 shows the spectral functions of the conduction band of *n*-doped STO, computed with the Migdal-Dyson formalism and the cumulant expansion. The doping is simulated by setting the Fermi level at 26 meV above the bare conduction band minimum (CBM), which corresponds to a charge carrier concentration of 1.6×10^{19} cm^{-3}. However, the energy renormalization of the bands brings the final polaronic CBM 10 meV below the Fermi level. This renormalization corresponds to an enhancement of the conduction band effective mass from its bare DFT value of 0.88 m_e to a renormalized value of 1.7 m_e, corresponding to a mass enhancement factor of $\lambda = 0.9$.

We see in Fig. 1 that the spectral function computed from both formalisms features a replica band. This satellite band emerges from the coupling of the conduction band to the dominant long-wavelength LO phonon modes, and signals the polaron formation. In the Migdal-Dyson formalism, it takes the form of a single sharp satellite peak, located at 115 meV below the conduction band minimum. In the cumulant expansion formalism, the satellite peak is broader, and situated at 94 meV below the CBM. This separation corresponds to the computed zone-center LO phonon frequency of 94.5 meV, which is the highest phonon branch of STO. The cumulant expansion formalism thus restores the physically expected separation of the satellite peak from the conduction band, which is overestimated in the Migdal-Dyson theory as discussed earlier. The cumulant result is consistent with ARPES studies in which replica bands are observed at the LO phonon frequency.

In Fig. 2, we compare the cumulant spectral function at Γ with the experimental ARPES spectrum from Ref. [2]. Our calculation nicely reproduces the "peak-dip-hump" feature, and the position of the secondary peak also agrees well with the experiment. This suggests that the observed replica band can be understood as a bulk property of STO. In addition to the main quasiparticle peak and the satellite, we observe another weaker peak between those two. We attribute this small peak to another LO phonon mode at 55 meV in STO, which also has a strong electron-phonon coupling. The relative strength of peaks does not agree perfectly with experiments. In our calculation, the ratio of the secondary peak intensity to the main peak is about 1/7, while in the experiment, it is about 1/2. There are several factors which can contribute to this discrepancy. First, the extrinsic effects in the photoemission experiment is not considered in our calculations. It has been shown that the extrinsic effects generally increases the strength of the replica bands and suppresses the main peak intensity [22]. Second, the photo-emission experiment is a surface sensitive technique. The reduction of screening effects on the surface could further enhance the satellite intensity. Having established that the cumulant expansion formalism can reproduce the spectral functions and polaronic features observed experimentally in STO, we turn our attention to the case of zinc oxide.

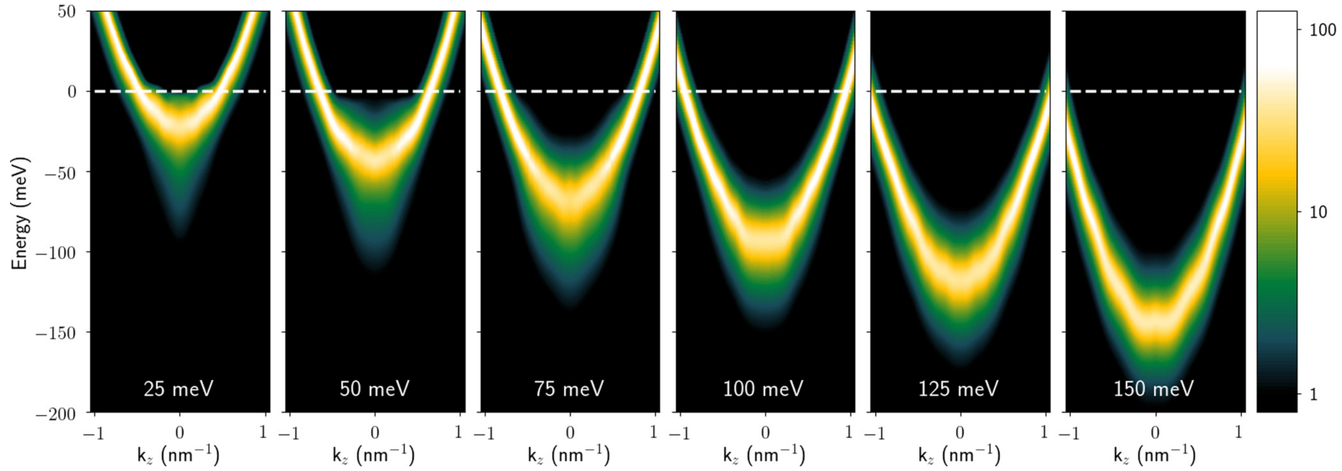

FIG. 3. Evolution of the spectral function of ZnO as a function of doping. The doping concentration is given by the indicated Fermi-level energy relative to the conduction band minimum shown in each panel.

B. ZnO

ARPES measurements on the surface of hydrogen-doped ZnO identified polaronic features in the spectra of the conduction band states, with a large tail extending over 400 meV [17]. To see whether these features arise in the bulk conduction band of ZnO, we compute the spectral function for several doping levels.

For undoped ZnO, we obtain a zero-point renormalization of the band gap of −157 meV, in excellent agreement with the experimental values obtained from mass derivatives (−164 meV) and from temperature-dependent absorption measurements (−156 meV) [39]. Again, the agreement of the computed zero-point band-gap renormalization with experiments gives us confidence in the accuracy of the electron-phonon coupling strength computed from DFPT. Figure 3 shows the evolution of the spectral function of the first conduction band of ZnO as a function of electron doping. The most important contributions to the self-energy come from the LO phonon branches with frequencies around 65 meV, which possess strong polar interactions, as well as from two TO modes with frequencies around 45 meV. The satellite bands associated with this coupling do not appear as distinct replicas, but rather as an elongated tail in the spectral function, which is nonetheless characteristic of a polaron. At dopings with Fermi level 50 meV above the conduction band minimum, kinks begin to appear in the bands, located one phonon frequency below the Fermi level. As the doping is further increased to 100 meV, these kinks lead to a flattening of the bottom of the conduction band. This process is enabled by the creation of a new scattering channel when the Fermi level relative to the bottom of the conduction band becomes larger than the LO phonon frequency. At this level of doping, holes at the bottom of the conduction band may interact strongly with other states below the Fermi level and of energy difference equal to the LO phonon frequency, thus enabling scattering events. At the same time, as the doping level increases, the extra carrier density becomes more effective at screening the phonon coupling potential. Without the metallic screening of the extra carriers, the electron-phonon coupling strengths of the polar modes have a characteristic $1/q$ dependence on the wave vector. However, the free carriers are especially effective at screening the macroscopic electric field induced by polar phonons, and the small-q divergence of the coupling strength is strongly attenuated. These two effects—the opening of new scattering channels and the long-wavelength screening—result in the flattening of the bottom of the conduction band at 100 meV doping and above.

A similar behavior has been identified in Fröhlich model calculations for strong coupling parameters, and signals the localization of the polaron [40]. Indeed, the qualitative change in the band dispersion and phonon-induced (polaronic) features as a function of doping can be interpreted as a transformation from a small-to-large polaron process. As doping increases, screening weakens the electron-phonon coupling and the system goes into the increasingly larger polaron regime.

Figure 4 shows the mass enhancement parameter λ of ZnO at different doping levels. It is obtained by fitting a quadratic dispersion to the renormalized band with an effective mass

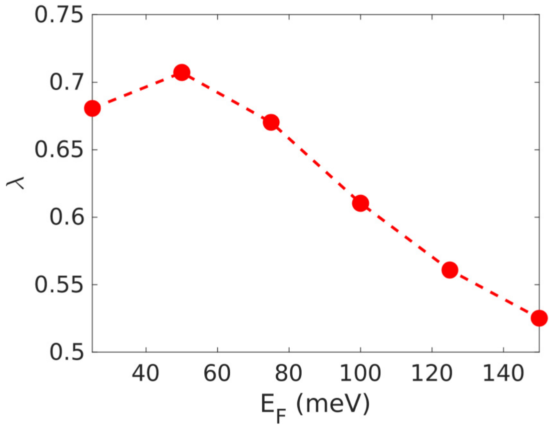

FIG. 4. Mass enhancement parameter λ of ZnO as a function of doping measured as the Fermi level relative to the conduction band minimum.

$m* = m_b(1+\lambda)$, where $m_b = 0.22$ is the bare effective mass from our DFT calculation. The effective mass reaches a maximum at doping near 50 meV since this doping level enables the scattering channel of the phonon branch with frequencies around 45 meV. At higher doping levels, these scattering channels are offset by the dielectric screening of the added charge carriers, which reduces the electron-phonon coupling strength and the mass renormalization.

IV. CONCLUSION

In summary, we studied from first principles the electron-phonon interactions in doped STO and ZnO that leads to the formation of polarons, and computed their corresponding spectral functions with the cumulant expansion formalism. In STO, the electron-phonon interaction leads to a large mass enhancement ($\lambda = 0.9$) and the formation of a distinct satellite band associated with the polaron. The spectral function matches well the ARPES measurements on doped STO surfaces. However, the satellite peaks associated with multi-phonon processes decay more rapidly than the ARPES signal, suggesting that surface effects and extrinsic effects would be needed to fully explain the measurements.

In ZnO, we do not find a distinct satellite band. Rather, the polaron manifests as kinks in the band dispersion, and a flattening of the bottom of the conduction band. As the doping level increases, the mass enhancement factors evolves in a nontrivial way. On the one hand, the opening of new scattering channels at doping resulting in a Fermi level higher than the phonon frequencies tend to increases the effective mass. On the other hand, the added charge carriers tend to screen the long-ranged electron-phonon coupling strength, thus reducing the mass renormalization of the bands. Overall, the effect of electron-phonon interaction in bulk ZnO cannot explain the large tail observed in ARPES measurements [17], which leads us to conclude that important surface effects may contribute to the experimental signals.

ACKNOWLEDGMENTS

This work was supported by the National Science Foundation under Grant No. DMR-1926004, which provided formalisms and theoretical analyses, and by the Center for Computational Study of Excited State Phenomena in Energy Materials, which is funded by the US Department of Energy, Office of Science, Basic Energy Sciences, Materials Sciences and Engineering Division under Contract No. DE-AC02-05CH11231, as part of the Computational Materials Sciences Program which provided advanced algorithms and codes. We acknowledge the use of computational resources at the National Energy Research Scientific Computing Center (NERSC), a DOE Office of Science User Facility supported by the Office of Science of the U.S. Department of Energy under Contract No. DE-AC02-05CH11231. The authors acknowledge fruitful discussions with Xavier Gonze, Lucia Reining, Philip B. Allen, Jean Paul Nery, Feliciano Giustino, Carla Verdi, Johannes Lischner and Derek Vigil-Fowler.

Y.-H.C. and G.A. contributed equally to this work.

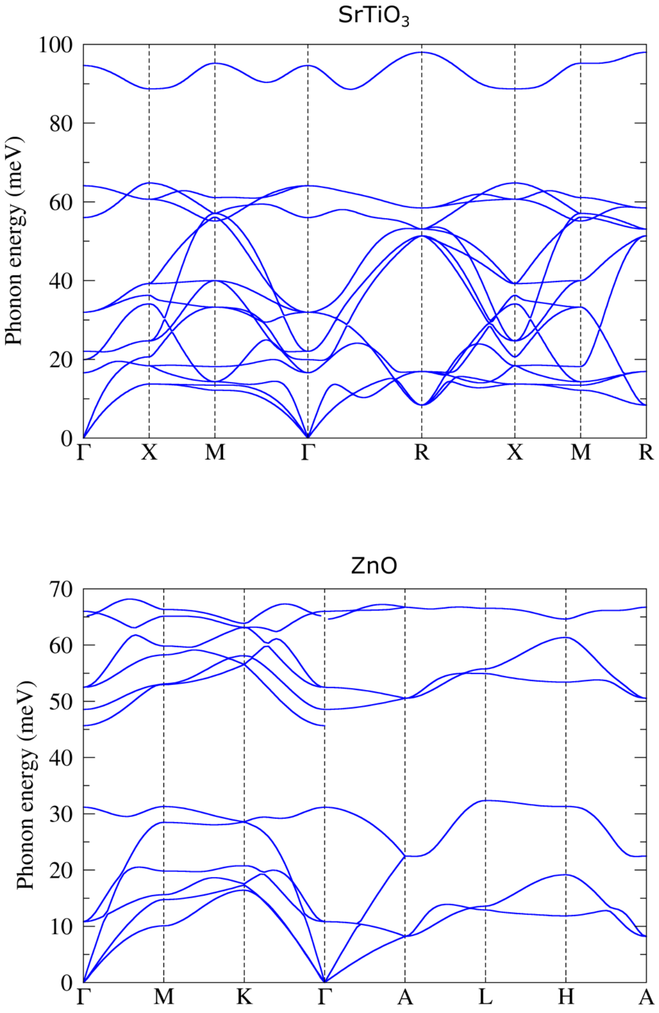

FIG. 5. Computed phonon band structure of STO (top) and ZnO (bottom).

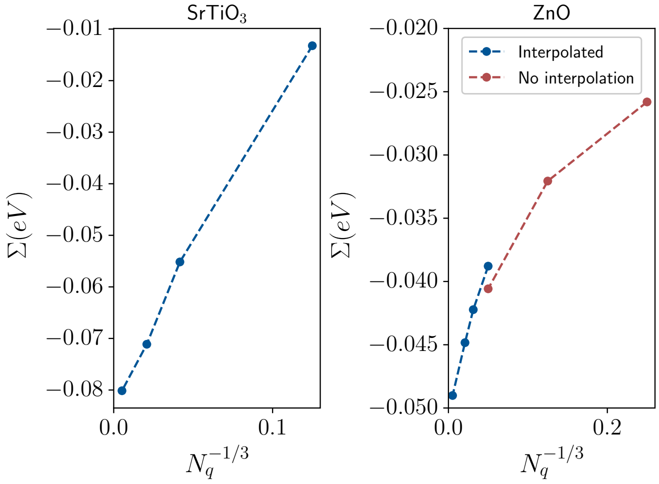

FIG. 6. Convergence of the self-energy with respect to the number of q-points (N_q) for the conduction band minimum of undoped STO (left) and undoped ZnO (right).

APPENDIX

Figure 5 shows the phonon band structures of STO and ZnO. For STO, we employ the TDEP method to stabilize the anharmonic phonon modes, as described in the method section. Our calculations agree well with previous work in Refs. [32,41]. The overall phonon dispersion of ZnO also agree with previous inelastic neutron scattering data [42,43] and DFT calculation [44] although our calculated LO phonon frequency 64 meV is slightly smaller than the reported experiment value 71 meV.

Figure 6 shows the convergence of the self-energy for the CBM of undoped STO and undoped ZnO. For ZnO, we compare the values from interpolated results with those from direct calculations. The difference between the interpolated result and noninterpolated one is less than 5 meV. With large **q** grid density, the self-energy converges linearly with the inverse of the number of q-points in one dimension.

---

[1] T. C. Rödel, F. Fortuna, S. Sengupta, E. Frantzeskakis, P. L. Fèvre, F. Bertran, B. Mercey, S. Matzen, G. Agnus, T. Maroutian *et al.*, Universal fabrication of 2D electron systems in functional oxides, Adv. Mater. **28**, 1976 (2016).

[2] C. Chen, J. Avila, E. Frantzeskakis, A. Levy, and M. C. Asensio, Observation of a two-dimensional liquid of Fröhlich polarons at the bare $SrTiO_3$ surface, Nat. Commun. **6**, 8585 (2015).

[3] A. F. Santander-Syro, O. Copie, T. Kondo, F. Fortuna, S. Pailhès, R. Weht, X. G. Qiu, F. Bertran, A. Nicolaou, A. Taleb-Ibrahimi *et al.*, Two-dimensional electron gas with universal subbands at the surface of $SrTiO_3$, Nature **469**, 189 (2011).

[4] W. Meevasana, P. D. C. King, R. H. He, S.-K. Mo, M. Hashimoto, A. Tamai, P. Songsiriritthigul, F. Baumberger, and Z.-X. Shen, Creation and control of a two-dimensional electron liquid at the bare $SrTiO_3$ surface, Nat. Mater. **10**, 114 (2011).

[5] L. F. J. Piper, A. R. H. Preston, A. Fedorov, S. W. Cho, A. DeMasi, and K. E. Smith, Direct evidence of metallicity at zno $(000\bar{1})$-(1×1) surfaces from angle-resolved photoemission spectroscopy, Phys. Rev. B **81**, 233305 (2010).

[6] S. Thiel, G. Hammerl, A. Schmehl, C. W. Schneider, and J. Mannhart, Tunable quasi-two-dimensional electron gases in oxide heterostructures, Science **313**, 1942 (2006).

[7] C. Cen, S. Thiel, G. Hammerl, C. W. Schneider, K. E. Andersen, C. S. Hellberg, J. Mannhart, and J. Levy, Nanoscale control of an interfacial metal–insulator transition at room temperature, Nat. Mater. **7**, 298 (2008).

[8] A. Brinkman, M. Huijben, M. van Zalk, J. Huijben, U. Zeitler, J. C. Maan, W. G. van der Wiel, G. Rijnders, D. H. A. Blank, and H. Hilgenkamp, Magnetic effects at the interface between non-magnetic oxides, Nat. Mater. **6**, 493 (2007).

[9] A. D. Caviglia, S. Gariglio, N. Reyren, D. Jaccard, T. Schneider, M. Gabay, S. Thiel, G. Hammerl, J. Mannhart, and J.-M. Triscone, Electric field control of the $LaAlO_3/SrTiO_3$ interface ground state, Nature **456**, 624 (2008).

[10] N. Reyren, S. Thiel, A. D. Caviglia, L. F. Kourkoutis, G. Hammerl, C. Richter, C. W. Schneider, T. Kopp, A.-S. Rüetschi, D. Jaccard *et al.*, Superconducting Interfaces Between Insulating Oxides, Science **317**, 1196 (2007).

[11] J.-J. Zhou and M. Bernardi, Predicting charge transport in the presence of polarons: The beyond-quasiparticle regime in $SrTiO_3$, Phys. Rev. Research **1**, 033138 (2019).

[12] J. P. Nery, P. B. Allen, G. Antonius, L. Reining, A. Miglio, and X. Gonze, Quasiparticles and phonon satellites in spectral functions of semiconductors and insulators: Cumulants applied to the full first-principles theory and the Fröhlich polaron, Phys. Rev. B **97**, 115145 (2018).

[13] R. I. Eglitis, E. A. Kotomin, G. Borstel, S. E. Kapphan, and V. S. Vikhnin, Semi-empirical calculations of the electronic and atomic structure of polarons and excitons in ABO_3 perovskite crystals, Comput. Mater. Sci. **27**, 81 (2003).

[14] R. I. Eglitis, *Ab Initio* calculations of $SrTiO_3$, $BaTiO_3$, $PbTiO_3$, $CaTiO_3$, $SrZrO_3$, $PbZrO_3$ and $BaZrO_3$ (001), (011) and (111) surfaces as well as F centers, polarons, KTN solid solutions and Nb impurities therein, Int. J. Mod. Phys. B **28**, 1430009 (2014).

[15] J. J. Lee, F. T. Schmitt, R. G. Moore, S. Johnston, Y.-T. Cui, W. Li, M. Yi, Z. K. Liu, M. Hashimoto, Y. Zhang *et al.*, Interfacial mode coupling as the origin of the enhancement of Tc in FeSe films on $SrTiO_3$, Nature **515**, 245 (2014).

[16] Z. Wang, S. M. Walker, A. Tamai, Y. Wang, Z. Ristic, F. Y. Bruno, A. de la Torre, S. Riccò, N. C. Plumb, M. Shi *et al.*, Tailoring the nature and strength of electron–phonon interactions in the $SrTiO_3$(001) 2D electron liquid, Nat. Mater. **15**, 835 (2016).

[17] R. Yukawa, K. Ozawa, S. Yamamoto, H. Iwasawa, K. Shimada, E. F. Schwier, K. Yoshimatsu, H. Kumigashira, H. Namatame, M. Taniguchi *et al.*, Phonon-dressed two-dimensional carriers on the ZnO surface, Phys. Rev. B **94**, 165313 (2016).

[18] S. Moser, L. Moreschini, J. Jaćimović, O. S. Barišić, H. Berger, A. Magrez, Y. J. Chang, K. S. Kim, A. Bostwick, E. Rotenberg *et al.*, Tunable Polaronic Conduction in Anatase TiO_2, Phys. Rev. Lett. **110**, 196403 (2013).

[19] O. Gunnarsson, V. Meden, and K. Schönhammer, Corrections to Migdal's theorem for spectral functions: A cumulant treatment of the time-dependent Green's function, Phys. Rev. B **50**, 10462 (1994).

[20] F. Aryasetiawan, L. Hedin, and K. Karlsson, Multiple Plasmon Satellites in Na and Al Spectral Functions from *Ab Initio* Cumulant Expansion, Phys. Rev. Lett. **77**, 2268 (1996).

[21] M. Guzzo, G. Lani, F. Sottile, P. Romaniello, M. Gatti, J. J. Kas, J. J. Rehr, M. G. Silly, F. Sirotti, and L. Reining, Valence Electron Photoemission Spectrum of Semiconductors: *Ab Initio* Description of Multiple Satellites, Phys. Rev. Lett. **107**, 166401 (2011).

[22] J. Lischner, D. Vigil-Fowler, and S. G. Louie, Physical Origin of Satellites in Photoemission of Doped Graphene: An *Ab Initio GW* Plus Cumulant Study, Phys. Rev. Lett. **110**, 146801 (2013).

[23] S. M. Story, J. J. Kas, F. D. Vila, M. J. Verstraete, and J. J. Rehr, Cumulant expansion for phonon contributions to the electron spectral function, Phys. Rev. B **90**, 195135 (2014).

[24] J. J. Kas, J. J. Rehr, and L. Reining, Cumulant expansion of the retarded one-electron Green function, Phys. Rev. B **90**, 085112 (2014).

[25] B. Gumhalter, V. Kovač, F. Caruso, H. Lambert, and F. Giustino, On the combined use of *GW* approximation and cumulant expansion in the calculations of quasiparticle spectra: The paradigm of Si valence bands, Phys. Rev. B **94**, 035103 (2016).

[26] J. McClain, J. Lischner, T. Watson, D. A. Matthews, E. Ronca, S. G. Louie, T. C. Berkelbach, and G. K.-L. Chan, Spectral functions of the uniform electron gas via coupled-cluster theory and comparison to the *GW* and related approximations, Phys. Rev. B **93**, 235139 (2016).

[27] C. Verdi, F. Caruso, and F. Giustino, Origin of the crossover from polarons to Fermi liquids in transition metal oxides, Nat. Commun. **8**, 15769 (2017).

[28] A. B. Migdal, Interaction between electrons and lattice vibrations in a normal metal, Sov. Phys. JETP **34**, 996 (1958).

[29] X. Gonze, B. Amadon, G. Antonius, F. Arnardi, L. Baguet, J.-M. Beuken, J. Bieder, F. Bottin, J. Bouchet, E. Bousquet *et al.*, The Abinit project: Impact, environment and recent developments, Comput. Phys. Commun. **248**, 107042 (2020).

[30] M. J. van Setten, M. Giantomassi, E. Bousquet, M. J. Verstraete, D. R. Hamann, X. Gonze, and G. M. Rignanese, The PseudoDojo: Training and grading a 85 element optimized norm-conserving pseudopotential table, Comput. Phys. Commun. **226**, 39 (2018).

[31] M. Guennou, P. Bouvier, J. Kreisel, and D. Machon, Pressure-temperature phase diagram of $SrTiO_3$ up to 53 GPa, Phys. Rev. B **81**, 054115 (2010).

[32] T. Tadano and S. Tsuneyuki, Self-consistent phonon calculations of lattice dynamical properties in cubic $SrTiO_3$ with first-principles anharmonic force constants, Phys. Rev. B **92**, 054301 (2015).

[33] T. Tadano and S. Tsuneyuki, *Ab initio* prediction of structural phase-transition temperature of $SrTiO_3$ from finite-temperature phonon calculation, J. Ceram. Soc. Jpn. **127**, 404 (2019).

[34] T. Tadano, Y. Gohda, and S. Tsuneyuki, Anharmonic force constants extracted from first-principles molecular dynamics: Applications to heat transfer simulations, J. Phys.: Condens. Matter **26**, 225402 (2014).

[35] C. Verdi and F. Giustino, Froehlich Electron-Phonon Vertex from First Principles, Phys. Rev. Lett. **115**, 176401 (2015).

[36] F. Brown-Altvater, G. Antonius, T. Rangel, M. Giantomassi, C. Draxl, X. Gonze, S. G. Louie, and J. B. Neaton, Band gap renormalization, carrier mobilities, and the electron-phonon self-energy in crystalline naphthalene, Phys. Rev. B **101**, 165102 (2020).

[37] A. Eiguren and C. Ambrosch-Draxl, Wannier interpolation scheme for phonon-induced potentials: Application to bulk MgB_2, W, and the (1x1) H-covered W(110) surface, Phys. Rev. B **78**, 045124 (2008).

[38] D. J. Kok, K. Irmscher, M. Naumann, C. Guguschev, Z. Galazka, and R. Uecker, Temperature-dependent optical absorption of $SrTiO_3$, Physica Status Solidi (a) **212**, 1880 (2015).

[39] M. Cardona and M. L. W. Thewalt, Isotope effects on the optical spectra of semiconductors, Rev. Mod. Phys. **77**, 1173 (2005).

[40] G. D. Mahan, *Many-Particle Physics*, 3rd ed. (Kluwer/Plenum, New York, 2000).

[41] J.-J. Zhou, O. Hellman, and M. Bernardi, Electron-Phonon Scattering in the Presence of Soft Modes and Electron Mobility in $SrTiO_3$ Perovskite from First Principles, Phys. Rev. Lett. **121**, 226603 (2018).

[42] A. Hewat, Lattice dynamics of ZnO and BeO, Solid State Commun. **8**, 187 (1970).

[43] K. Thoma, B. Dorner, G. Duesing, and W. Wegener, Lattice dynamics of ZnO, Solid State Commun. **15**, 1111 (1974).

[44] J. Serrano, F. J. Manjón, A. H. Romero, A. Ivanov, M. Cardona, R. Lauck, A. Bosak, and M. Krisch, Phonon dispersion relations of zinc oxide: Inelastic neutron scattering and *ab initio* calculations, Phys. Rev. B **81**, 174304 (2010).